

Domain decomposition of the modified Born series approach for large-scale wave propagation simulations

Swapnil Mache^{a,1}, Ivo M. Vellekoop^{a,*}

^a*Biomedical Photonic Imaging Group, Faculty of Science and Technology, University of Twente, P.O. Box 217, Enschede, 7500 AE, The Netherlands*

Abstract

The modified Born series method is a fast and accurate method for simulating wave propagation in complex structures. Currently, its main limitation is that the simulation size is limited by the working memory of a single computer or graphics processing unit (GPU). Here, we present a domain decomposition method that removes this limitation. We show how to decompose large problems over subdomains while maintaining the method's accuracy, memory efficiency, and guaranteed monotonic convergence. We demonstrate our approach by solving the Helmholtz problem for a complex structure of size $315 \times 315 \times 315$ wavelengths in just 1.4 hours on a dual-GPU system.

Keywords: Helmholtz equation, Born series, modified Born series, Domain decomposition

1. Introduction

Wave propagation simulations have many applications, ranging from nanophotonics to geophysics. Unfortunately, computing accurate solutions to wave equations in large heterogeneous media is highly time-consuming. A great number of numerical methods are available for solving wave equations in heterogeneous media [1]. One of the fastest and most accurate methods is the modified Born Series (MBS) [2, 3]. It represents the structure on a regular grid, allowing arbitrarily complex structures to be defined.

*Corresponding author. *E-mail address:* i.m.vellekoop@utwente.nl (I. M. Vellekoop)

¹Present address: Rayfos Ltd., Winton House, Winton Square, Basingstoke, United Kingdom

Unlike widely used methods such as the finite-difference time-domain (FDTD) [4, 5, 6, 7] and pseudospectral time-domain (PSTD) [8, 9, 10] methods, the MBS does not rely on finite difference approximations. This is an important benefit since the finite difference approximations accumulate as the wave propagates, easily causing errors of more than 1% per propagated wavelength [11], meaning that the relative phase of two beams can be off by π already after 50 wavelengths. The numerical dispersion of finite approximations is well-studied in literature [8, 12, 13, 14].

An additional benefit of MBS is that it requires far fewer iteration steps than FDTD or PSTD methods [2]. These combined benefits currently make the MBS one of the most efficient methods to solve Helmholtz and Maxwell’s equations [2, 15], with subsequent extensions to birefringent media [16], the inverse scattering problem [17], and applications to photoacoustics [18] and geophysics [19]. Transient wave phenomena, which are especially important in sound and seismic waves, can be simulated by solving for each frequency component individually, as is common in frequency-domain methods [20, 21, 22, 23, 24, 25]. This approach has the advantage of being able to accurately describe physical dispersion effects (i.e. wavelength-dependent propagation speed).

Osnabrugge et al. [3] showed that the MBS could be executed on a graphics processing unit (GPU) efficiently, solving Maxwell’s equations in a structure of $28 \times 28 \times 28$ wavelengths in just 3 seconds, representing a factor of 50 speed-up compared to performing the simulations on a central processing unit (CPU). Recently, Valantinas and Vettenburg [26] solved the Helmholtz equation for a system of $2.1 \cdot 10^7$ cubic wavelengths by mapping the steps of the MBS to layers in an artificial neural network framework, leveraging the extensive software and hardware acceleration available for these applications. However, GPUs have a limited amount of expensive working memory. They cannot be expanded as flexibly as the main working memory, adding a severe limitation to the simulation size [27, 28].

For FDTD, this problem has been solved by domain decomposition, i.e., by distributing the computations over multiple PCs or GPUs, each solving a subdomain of the original problem [29, 30, 31, 32]. This approach enables simulations of arbitrary size, limited only by the total memory available in a cluster or multi-GPU PC.

Here, we present a domain decomposition approach for the MBS to solve the Helmholtz equation. Our approach, based on a non-overlapping domain decomposition strategy [33, 34, 35, 36], maintains the key benefits of MBS:

low memory use, high accuracy, and guaranteed convergence, while minimising the overhead on memory use and computation time. Whereas it is common to explicitly formulate boundary conditions for the wave equation [36, 37, 38], our approach implicitly handles both the external boundary conditions and the boundary conditions at the domain boundaries, allowing both periodic and non-periodic boundaries. At the exterior, these boundaries are combined with a thin absorbing anti-reflection layer [3], eliminating the need for computationally expensive padding with thick absorbing boundary layers [8, 37].

We demonstrate the domain decomposition approach on a dual-GPU system through a large 3D simulation of $3.1 \cdot 10^7$ cubic wavelengths, a size that is $1.93\times$ larger than the maximum that could be accommodated on a single GPU and took only 1.4 hours to complete. An open-source implementation in Python is available on GitHub [39].

We start in Section 2 by summarising the MBS approach. In Section 3, we introduce the proposed domain decomposition method. We then demonstrate the approach and analyse its efficiency and accuracy (Section 4). Concluding remarks are provided in Section 5.

2. Modified Born series

This section summarises the MBS approach introduced by Osnabrugge et al. [2], using the simplified formalism introduced in [40]. Consider the inhomogeneous Helmholtz equation

$$[\nabla^2 + k^2(\mathbf{r})] x(\mathbf{r}) = -y(\mathbf{r}), \quad (1)$$

where $k(\mathbf{r})$ is the wavenumber, $x(\mathbf{r})$ is the field, and $y(\mathbf{r})$ is the source term as a function of the position vector \mathbf{r} . For convenience, we introduce the notation

$$A\mathbf{x} = \mathbf{y}, \quad (2)$$

where linear operator $A := c[\nabla^2 + k^2(\mathbf{r})]$ is the left-hand side of the Helmholtz equation and vectors $\mathbf{x} := x(\mathbf{r})$ and $\mathbf{y} := -cy(\mathbf{r})$ represent the solution and the source, respectively. c is a scaling factor that is discussed below.

The key step in both the modified [2] and original [41] Born series formalisms is to split $A = L + V$, with $L := c[\nabla^2 + k_0^2]$ corresponding to wave propagation in a homogeneous medium with background wavenumber k_0 , and $V = c[k^2(\mathbf{r}) - k_0^2]$ the scattering potential.

The MBS method uses this splitting to define a preconditioned Richardson iteration [40]

$$\mathbf{x}^{(n+1)} = \mathbf{x}^{(n)} + \alpha \Gamma^{-1} (\mathbf{y} - A\mathbf{x}^{(n)}), \quad (3)$$

where n is the iteration counter and $\Gamma = (L + I)(I - V)^{-1}$ is the preconditioner. The constant α is called the relaxation parameter [42, 43, 44].

In contrast to the original Born series, which diverges for large or strongly scattering media [45], the MBS converges monotonically to the solution of Eq. (1) provided that $\alpha \leq 1$ and ic is a real number less than $1/|k^2(\mathbf{r}) - k_0^2|_\infty$ [2], where $|\cdot|_\infty$ denotes the maximum value over all \mathbf{r} . We can truncate this iteration when the norm of the residual $\Gamma^{-1} (\mathbf{y} - A\mathbf{x}^{(n)})$ drops below a certain threshold.

A further refinement to optimise the convergence rate was given in [40], leading to the choices

$$c = -\frac{0.95i}{\|k^2(\mathbf{r}) - k_0^2\|_\infty}, \quad \alpha = 0.75. \quad (4)$$

The splitting $A = L + V$ is visualised in Fig. 1a-c, where the operators are represented as matrices for illustrative purposes. In practice, these operators are not implemented as matrices since the full matrices would be too large to store in memory. The alternative of using sparse matrices would require replacing L by a matrix with only a few diagonals, which is precisely the finite difference approximation that causes numerical dispersion and thus should be avoided. Instead, L can be implemented as a convolution with the angular spectrum kernel [46, 47]

$$L = c\mathcal{F}^{-1} (-\|\mathbf{p}\|^2 + k_0^2) \mathcal{F}, \quad (5)$$

where \mathcal{F} and \mathcal{F}^{-1} denote the forward and inverse Fourier transform, respectively, and \mathbf{p} denotes the Fourier-space coordinate vector. In practice, a fast Fourier transform is used to evaluate this convolution efficiently. As shown in Fig. 1d, this approach does introduce wrapping artefacts. These artefacts can be significantly reduced by using an alternating sequence of offset Fourier transforms [3] and eliminated using our proposed method (see Section 3). Either of these methods is then combined with a thin absorbing boundary layer to ensure convergence [3].

Similar to Eq. (5), we can implement $(L + I)^{-1}$ as a (fast) convolution. Substituting $\Gamma^{-1} = (I - V)(L + I)^{-1}$ and $A = (L + I) - (I - V)$ into Eq. (3)

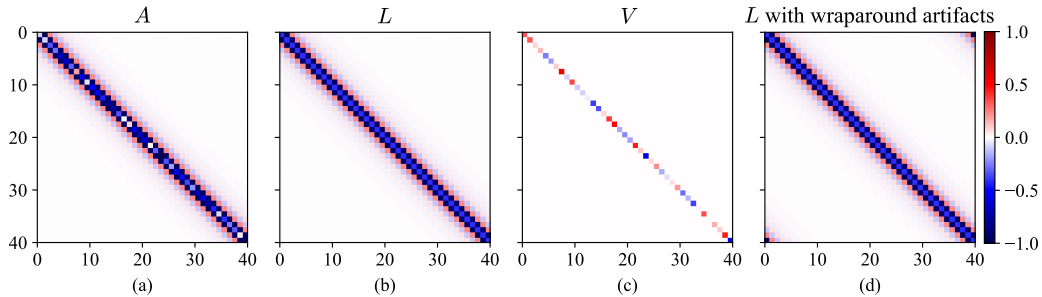


Figure 1: Matrix representation of splitting operator A into $L + V$ for a 1D system. (a) Operator A is split into (b) L containing the Laplacian operator, a band along the diagonal, and (c) V , a diagonal matrix containing the scattering potential. (d) The operator L with wraparound artefacts resulting from implementing L as a fast convolution (Eq. (5)).

gives the iteration [2]

$$\mathbf{x}^{(n+1)} = \mathbf{x}^{(n)} - \alpha(I - V) (\mathbf{x}^{(n)} - (L + I)^{-1} [\mathbf{y} + (1 - V)\mathbf{x}^{(n)}]), \quad (6)$$

which requires only one fast convolution per iteration. This is another important benefit of the MBS: the preconditioned operator $\Gamma^{-1}A$ can be evaluated at almost no extra cost compared to the original operator A , which also requires a single fast convolution.

3. Domain decomposition of the modified Born series

We start by decomposing the linear system $A\mathbf{x} = \mathbf{y}$ over multiple subdomains. For illustrative purposes, we decompose a 1D problem into two subdomains of equal size N . The same strategy extends to 2D and 3D problems, with any number of subdomains along any dimension and domains of unequal size. The operator A for this 1D problem can be represented as a block matrix:

$$\begin{bmatrix} A_{11} & A_{12} \\ A_{21} & A_{22} \end{bmatrix} \begin{bmatrix} \mathbf{x}_1 \\ \mathbf{x}_2 \end{bmatrix} = \begin{bmatrix} \mathbf{y}_1 \\ \mathbf{y}_2 \end{bmatrix}, \quad (7)$$

where the blocks A_{11} , A_{12} , A_{21} , and A_{22} are of size $N \times N$, and the vectors \mathbf{x}_1 , \mathbf{x}_2 , \mathbf{y}_1 , and \mathbf{y}_2 are of length N . Here, A_{11} and A_{22} are matrices operating on the two subdomains, while the blocks A_{12} and A_{21} represent information

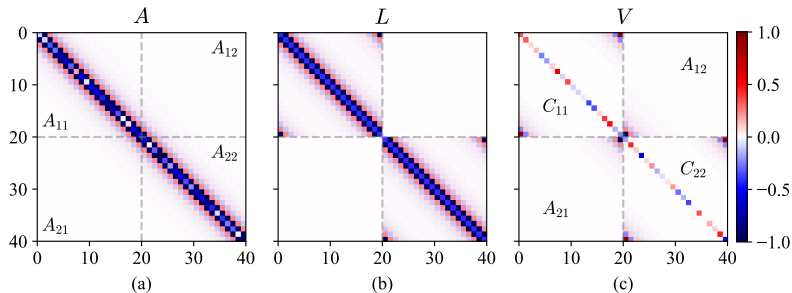


Figure 2: Matrix representation of domain decomposition. (a) A (same as Fig. 1a) is decomposed over two subdomains, shown by the grey lines. (b) Decomposition of L , implemented as a fast convolution (Eq. (5)) over each subdomain, thus containing wraparound artefacts. The off-diagonal communication blocks are empty. (c) $V := A - L$ contains the scattering potential on the diagonal and the wraparound and communications corrections.

transfer between the subdomains. The matrix representation of the decomposition of A over two subdomains is shown in Fig. 2a.

An essential generalisation of the MBS introduced in [40] is that we have complete freedom to choose the splitting $A = L + V$, as long as the scaling factor c can be selected such that $\|V\| < 1$. We use this freedom to implement our domain decomposition framework.

This freedom enables us to implement L as a fast convolution over each subdomain (see Fig. 2b). Representing L and V in block matrix form

$$L = \begin{bmatrix} L_{11} & 0 \\ 0 & L_{22} \end{bmatrix}, \quad V = \begin{bmatrix} A_{11} - L_{11} & A_{12} \\ A_{21} & A_{22} - L_{22} \end{bmatrix}, \quad (8)$$

we see that L is a domain-local operator and V is mostly domain-local, with small, explicit contributions for transfer between domains (represented by A_{12} and A_{21} , also seen in Fig. 2c). It is important to note that the system being solved here is still the same as in Eq. (2).

In L (Eq. (8)), the diagonal blocks L_{11} and L_{22} (visualized in Fig. 2b) contain wraparound artefacts, similar to Fig. 1d. These wraparound artefacts appear in V with the opposite sign, as $V := A - L$. V now has three contributions (Fig. 2c). The domain-local part constitutes the original scattering potential on the diagonal and the correction for the wrapping artefacts caused by the fast convolution, which we call C_{11} and C_{22} . The non-local part of V is the off-diagonal blocks A_{12} and A_{21} representing communication between the subdomains.

The interior subdomain communication and exterior boundary corrections are based on these matrices C_{11} , C_{22} , A_{12} , and A_{21} combined with a thin absorbing boundary layer [3] on the exterior. For the exterior boundary, the matrices C_{11} and C_{22} are used to tackle the wrapping artefacts, which allows for only a thin absorbing boundary layer to minimize reflection artefacts. For the interior boundaries, we use the matrices C_{11} and C_{22} to tackle the wrapping artefacts at the interface between subdomains, and the matrices A_{12} and A_{21} for communication between the subdomains.

Thus, our approach does not require explicit steps to guarantee continuity at the subdomain boundaries but instead results in the naturally occurring boundary conditions at the interface through the matrices A_{12} and A_{21} . The matrices C_{11} , C_{22} , A_{12} , and A_{21} can all be constructed directly by comparing two situations: 1) the angular spectrum kernel applied to a point source using a linear convolution (Fig. 3a), and 2) the same kernel applied using a fast convolution on a subdomain (Fig. 3b). The difference between these two curves gives the required wrapping correction (which corresponds to a column of matrix C_{11}) and the transfer to the second subdomain (a column of matrix A_{12}). By repeating this process for different positions of the point source and thus different columns of the matrices, we recover matrices C_{11} and A_{12} . Due to the symmetry of the angular spectrum kernel, the bottom-left part of matrix C_{11} is equal to $-A_{12}$. The top-right part of matrix C_{11} is given by the transpose $-A_{12}^T$.

Figure 3c visualizes the bottom-left part of the domain-transfer matrix A_{12} (also see Fig. 2c), which shows that the magnitude of the elements decreases rapidly away from the subdomain border. Therefore, we can truncate matrices C and off-diagonal blocks of A to only consider $t \ll N$ edge points near the boundaries. This way, the overhead of these additional computations is minimised.

Fig. 4 visualises the truncated corrections in V for the same example as Fig. 2. The operator A obtained using the truncated corrections is shown in Fig. 4a. The decomposed operator L (Eq. (8)) shown in Fig. 4b remains unchanged irrespective of the truncation and is the same as in Fig. 2b. Fig. 4c shows the matrix representation of the operator V obtained using the truncated corrections instead of the full corrections as in Fig. 2d. The effect of the truncation is visible in Fig. 4c as square blocks of size $t = 6$.

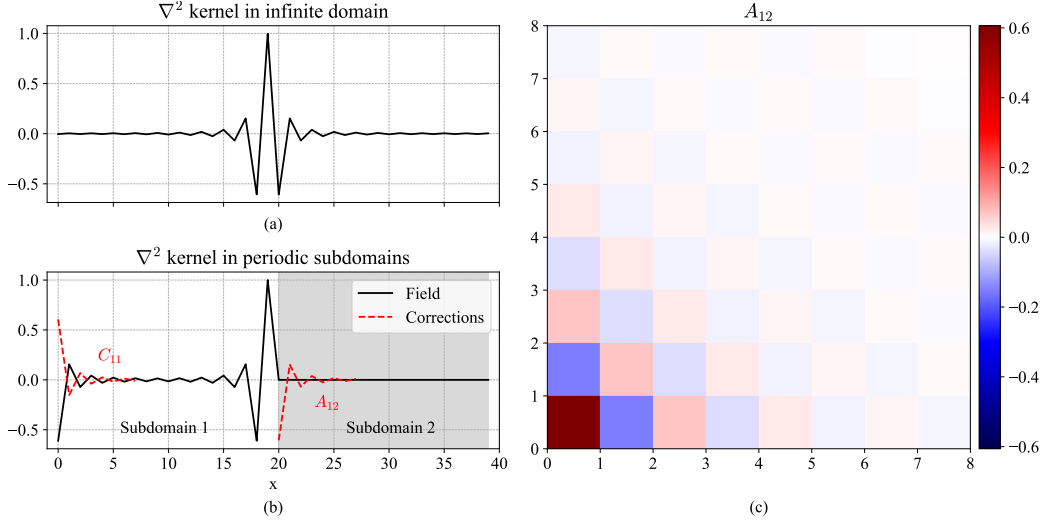


Figure 3: Generation of the matrix A_{12} for wrapping and transfer corrections. (a) Field after convolution of the Laplacian with a point source. (b) Field when the fast convolution is computed only over Subdomain 1 (white background). The difference between the fields in (a) and (b) is shown by the dashed red lines and gives columns of (c) the (truncated) correction matrix A_{12} .

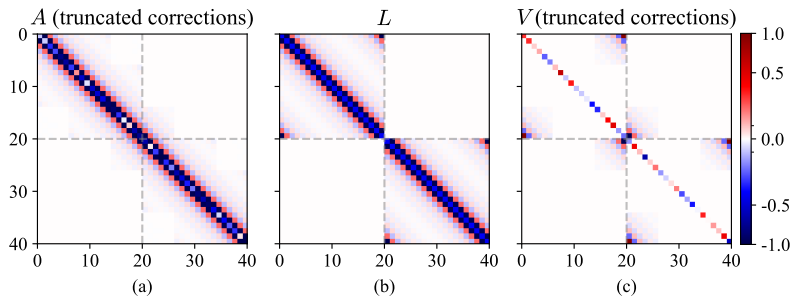


Figure 4: Using truncated corrections in V to reconstruct A . (a) Matrix representation of A decomposed over two subdomains, demarcated by the dashed grey lines, but with truncated corrections. (b) L decomposed over the subdomains remains unchanged and is the same as in Fig.2b. (c) V with truncated corrections for wrapping and transfer, visible as square blocks of side $t = 6$ in the corners of subdomain blocks. Note that the colour scale is logarithmic in both the positive and negative directions from 0.

3.1. Implementation

The domain decomposition framework is incorporated into the preconditioned Richardson iteration Eq. (6), but with the operators L and V computed for and applied to each subdomain. Thus, the fast convolution with $(L + I)^{-1}$ is computed for each subdomain s as $(L_s + I)^{-1}$. It is the same for all subdomains of the same size and needs to be computed only once in that case. As discussed in Section 3, operator V has three contributions, i.e. the scattering potential on the diagonal, which is now applied over the subdomains, the wrapping corrections C , and the transfer corrections (off-diagonal blocks of A). The steps for computing and applying the operator V for every subdomain s are as below:

1. Compute corrections ($C_{ss}\mathbf{x}_s$) for all edges based on the correction matrix C_{ss} (described in Section 3). Note that C_{ss} is a highly sparse matrix as the correction is truncated to $t \ll N$ points at the edge of the subdomain.
2. Transfer these edge corrections to the neighbouring subdomains.
3. Apply the scattering potential.
4. *Add* the edge corrections from the current subdomain, corresponding to the wrapping corrections C_{ss} .
5. *Subtract* the edge corrections coming from the neighbouring subdomains, which correspond to the transfer corrections $A_{s,s\pm 1}$, where the subscript $s \pm 1$ represents the neighbouring subdomains.

We define the relative residual $\epsilon := \|\Gamma^{-1}(\mathbf{y} - A\mathbf{x}^{(n)})\| / \|\Gamma^{-1}\mathbf{y}\|$, where $\|\cdot\|$ is the Euclidean norm. For the domain decomposition case, the global residual is given by $\sqrt{\sum_s \epsilon_s^2}$, where the summation is over all subdomains s . We use a threshold value 10^{-6} as the stopping criterion. After the iteration has converged, the fields from the different subdomains are combined to give the final solution of the global field \mathbf{x} .

Since we now use a different operator V than the original MBS implementation, we can no longer use Eq. (4) to compute the scale factor c . Instead, we now require $ic < 1/\|V\|$, where $\|V\|$ denotes the operator norm of V , i.e. its largest singular value [40]. For simplicity, we estimate this norm as the sum of the norms of all contributions to V : the original scattering potential, the wrapping correction, and domain transfer components, which gives an upper limit for $\|V\|$ and results in a scaling factor of

$$c = \frac{0.95i}{\|k^2(\mathbf{r}) - k_0^2\|_\infty + (\sum_{d=1}^3 a_d) \|A_{12}\|}, \quad (9)$$

where a_d equals 0 if no wrapping or transfer correction is applied along dimension d (corresponding to periodic boundaries). It equals 1 if only wrapping corrections are needed (i.e. when there is only a single subdomain along this dimension) and 2 if both the wrapping and transfer corrections are used. Thus, the wrapping and transfer corrections reduce the value of c , leading to slower convergence when $a_d \neq 0$. For a 1-domain simulation without wrapping corrections, $a_d = 0$, and Eq. (9) reduces to Eq. (4).

Domain decomposition also offers an opportunity to improve the efficiency of the computations by initially activating only those subdomains that hold a source term. Neighbouring subdomains are activated only after the norm of the transferred field exceeds a certain threshold. Although this initially causes a small error, the MBS converges to the correct solution from any starting point and thus nullifies these errors.

With this activation strategy, for example, a 3D simulation of size $100 \times 100 \times 100$ wavelengths split into $3 \times 1 \times 1$ subdomains was 12% faster than without this strategy.

4. Results and Discussion

In this section, we demonstrate the domain decomposition of the MBS in 3D simulations. For all simulations in this section, we simulate light propagation through a scattering structure illuminated with a planar source located at $x = 0$. We use absorbing boundaries with a thickness of 5 wavelengths [3], and a sampling of 4 points per wavelength.

The structure consists of tightly packed spheres, with a relative wave velocity (or refractive index) of 1.33 and a small imaginary part, distributed randomly in a medium with a refractive index $n = 1$. The spheres were generated using the `random_spheres()` function in PoreSpy [48]. Unless stated otherwise, we used spheres of radius 3 wavelengths and a truncation size of $t = 8$ in the simulations.

We start by validating the domain decomposition framework on a small sample and then analyse the accuracy and convergence of the domain decomposition approach for different truncation sizes t and numbers of subdomains. Finally, we demonstrate domain decomposition in a large structure of $3.1 \cdot 10^7$ cubic wavelengths.

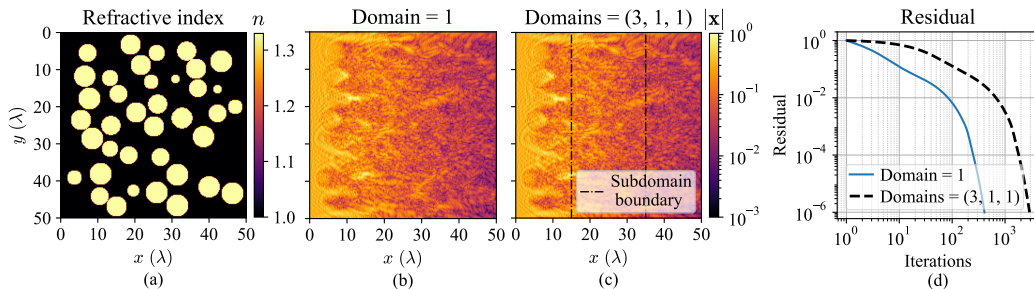


Figure 5: Simulation results with and without domain decomposition for a 3D medium of size $50 \times 50 \times 50$ wavelengths. 2D slices at $z/2$ of (a) the refractive index distribution used in the simulation, (b) the result for a single domain, and (c) the result with three subdomains in the x direction, with the dash-dotted black lines indicating the subdomain boundaries. (d) Residual vs. iteration number for the simulations in b (solid blue line) and c (dashed black line).

4.1. Domain decomposition validation

We first validate the accuracy of our domain decomposition framework by comparing it to the single-domain MBS approach for a 3D simulation of size $50 \times 50 \times 50$ wavelengths. We quantify the accuracy by comparing the field obtained from domain decomposition (\mathbf{x}) and the single-domain simulation result (\mathbf{x}_{ref}) with the relative error $\|\mathbf{x} - \mathbf{x}_{\text{ref}}\|^2 / \|\mathbf{x}_{\text{ref}}\|^2$, where $\|\cdot\|$ denotes the Euclidean norm over all elements in the field array excluding the absorbing boundaries.

Fig. 5a shows a slice, through the centre of the z -axis, of the 3D refractive index distribution used in this test. The results of the simulations are shown in Fig. 5b for the single domain and in Fig. 5c for the domain decomposed into three subdomains along the x -axis. The relative error between the two is just $1.7 \cdot 10^{-4}$, confirming the validity of our domain decomposition approach.

Fig. 5d shows the residual as a function of the iteration number for the two simulations. It can be seen that the residual decreases monotonically, which is a key property of the MBS. The single-domain simulation converged in 409 iterations in 2.3 seconds, while the 3-domain simulation converged in 2,908 iterations in 11.7 seconds. The $7\times$ increase in the number of iterations is due to a lower scaling coefficient c , with $a_d = 2$ (Eq. (9)). Although this is a significant increase in the number of iterations, this factor is independent of the number of subdomains along an axis, as we will analyse in more detail in Section 4.2.2.

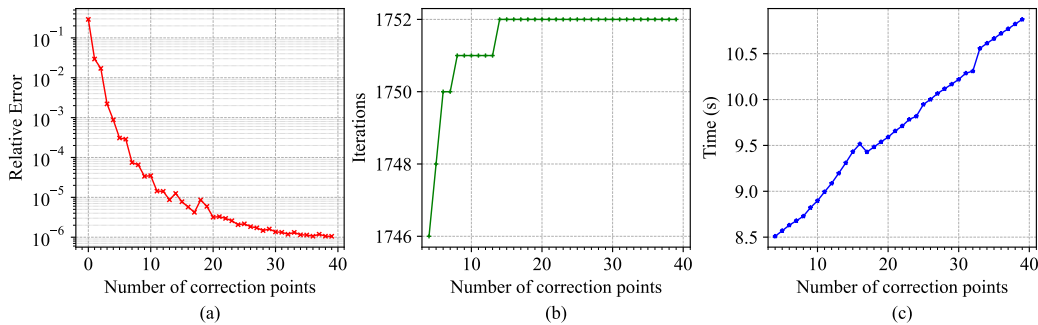


Figure 6: Convergence of a 3D simulation with two subdomains for different numbers of correction points t . (a) Relative error with a 1-domain simulation decays with t . (b) The number of iterations is almost constant for $t = 4$ and higher, showing no dependence on t . (c) The total simulation time in seconds consistently increases for more correction points.

4.2. Convergence dependence on truncation parameter and number of subdomains

In this section, we test the convergence behaviour of the domain decomposition simulations and the dependence on the truncation parameter and number of subdomains using the same structure as before.

4.2.1. Dependence on truncation parameter

First, we examine the convergence behaviour as a function of t , the number of correction points used to generate the correction matrices C_{11} and A_{12} (Section 3). We decomposed the problem in Section 4.1 into two subdomains along the x-axis and varied t from 0, indicating no correction, to 40. We compare the relative error of these simulations with a single-domain simulation, as shown in Fig. 6a. The relative error between the two decays with more correction points, and with just $t = 4$, the error is already less than 0.1%.

Fig. 6b shows the number of iterations for convergence as a function of the number of correction points, plotted for $t = 4$ and higher, as the accuracy is low for $t < 4$. The figure shows that the number of iterations does not depend on t . The time for convergence (Fig. 6c) consistently increases with more correction points, which is expected since the size of the correction matrix increases.

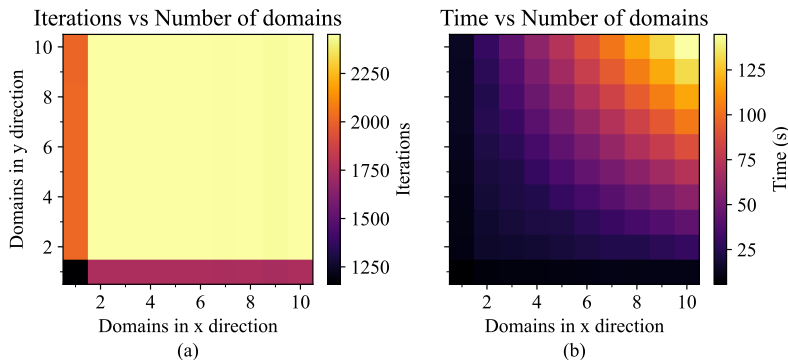


Figure 7: Number of iterations (a) and time (b) as a function of the number of subdomains along the x and y directions for a 3D simulation. The iteration count increases considerably only when subdomains are added along a new axis. The time increases with the number of subdomains but is consistently low for one domain in either x *or* y direction.

4.2.2. Dependence on number of subdomains

Next, we examine the number of iterations and time as a function of the number of subdomains (Fig. 7). Fig 7a shows the number of iterations for different numbers of subdomains along the x and y-axis. The lowest number of iterations (1160) is for a 1-domain simulation (black pixel in the lower left corner in Fig. 7a). This case corresponds to a scaling coefficient c based on only a wrapping correction along the x-axis, for which the system is non-periodic. When there is more than one subdomain along *either* the x or y-axis, the scaling factor c reduces, which increases the iterations to around 1751 with more domains along the x-axis (dark pink band of pixels for $y = 1$ in Fig. 7a), and around 2018 for more domains along the y-axis (orange band of pixels for $x = 1$ in Fig. 7a). For more than one subdomain in *both* the x and y direction, scaling coefficient c is even lower, increasing the iterations to around 2448 (Fig. 7a, the light yellow pixels for x and $y > 1$). Thus, the number of iterations increases only when subdomains are added along a new axis. The number of iterations is not dependent on the number of subdomains beyond one along an axis.

Fig. 7b shows the simulation time in seconds as a function of the number of subdomains along the x and y-axis. The simulation time is consistently low for one domain in x *or* y directions (black band of pixels along the x and y axes at $x = 1$ or $y = 1$). It consistently increases with more subdomains due to an increase in the amount of communication between them. The time is highest for 10 domains along both x *and* y directions, i.e., the total number

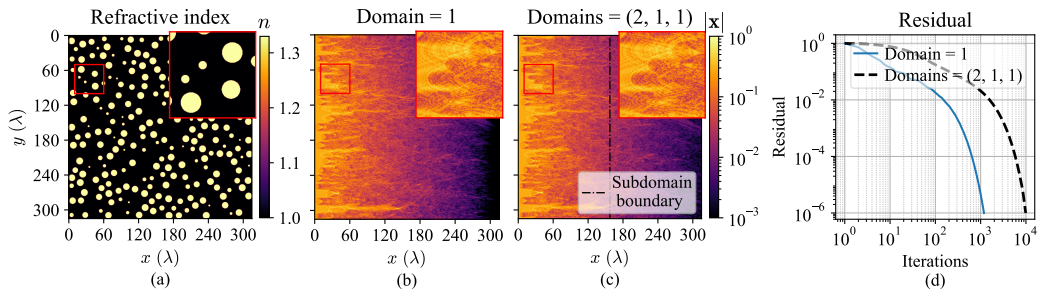


Figure 8: Large 3D simulation of size $315 \times 315 \times 315$ wavelengths with and without domain decomposition. A 2D slice of (a) the refractive index map, (b) the result from a 1-domain simulation on the CPU, and (c) the result from a 2-domain simulation using two GPUs, with the dash-dotted black line indicating the subdomain boundary. The insets are zoomed-in portions of the selected area to show finer details. (d) Residual as a function of the iterations for (b), a solid line, and (c), a dashed line.

of subdomains = 100 (top right corner of Fig. 7b).

4.3. Large scale simulations

To demonstrate the larger simulation size enabled by the domain decomposition approach, we run a simulation of $3.1 \cdot 10^7$ cubic wavelengths on a system with an AMD EPYC 9354P CPU @ 3.25 GHz with 256 GB RAM and two GPUs (both NVIDIA L40S 48GB). The structure is the same as mentioned at the beginning of Section 4, except that the spheres have a radius of 6 wavelengths and the clearance between them is set to 6 wavelengths, which helps the energy propagate deeper into the simulation away from the source. The simulation size is a much larger $315 \times 315 \times 315$ wavelengths, corresponding to $1260 \times 1260 \times 1260$ voxels. Due to this large size, the simulation cannot be performed on a single GPU. Therefore, we run the single-domain simulation on the CPU and compare it against the 2-domain, 2-GPU simulation performed with the same system.

Fig. 8a shows a slice, through the centre of the z-axis, of the 3D refractive index map used. The single-domain and 2-domain simulation results are shown in Figs. 8b and c, respectively. The insets in Fig. 8a-c show finer details in a zoomed-in region of the slices. The relative error between the two is $2.5 \cdot 10^{-4}$.

Fig. 8d shows the residual as a function of the iterations for the two simulations. The two-domain simulation converges in 9,878 iterations in 1.4 hours (4,958 s), while the single-domain simulation converges in 1,181

Run parameters	Total size (cubic wavelengths)	Time (s)	Iterations
2 domains, 2 GPUs	$3.1 \cdot 10^7$	4,958.65	9,878
1 domain, CPU	$3.1 \cdot 10^7$	65,537.16	1,181

Table 1: The largest possible simulation with domain decomposition, using 2 GPUs, and without, using the CPU. The simulations were run on a system with an AMD EPYC 9354P CPU @ 3.25 GHz with 256 GB RAM and two GPUs (both NVIDIA L40S 48GB). The domain decomposition simulation (row 1) takes $8.3\times$ the number of iterations for convergence as the CPU simulation (row 2) but is $13.2\times$ faster.

iterations in 18.2 hours (65,537 s) since it is run on the CPU (Table 1).

In the 2-domain case, the wrapping and transfer corrections lower the scaling coefficient c , increasing the number of iterations by $8.3\times$. In addition to this increase in the number of iterations, the domain decomposition framework has two overheads: the overhead of computing the edge corrections and the overhead due to data transfer between GPUs when the edge corrections are transferred and applied to neighbouring subdomains in each iteration. This subdomain communication leads to a lock-step execution, meaning the GPUs wait for the results of the other GPU(s). This overhead adds approximately 40% time per cubic wavelength and reduces for larger simulations.

Despite this overhead, the 2-domain, 2-GPU simulation is $13.2\times$ faster than the single-domain simulation on the CPU without domain decomposition. With these two GPUs, we increased the simulation size by $1.93\times$ of what can be accommodated on a single GPU to an unprecedented $315 \times 315 \times 315$ wavelengths. Furthermore, we showed that the number of domains can be increased arbitrarily. The overhead of adding additional domains is much smaller than the initial step from one to two subdomains, especially when the domain is split into subdomains along a single axis.

5. Conclusion

We have introduced a domain decomposition of the modified Born series (MBS) approach [2, 40] applied to the Helmholtz equation. With the new framework, we simulated a complex 3D structure of a remarkable $3.1 \cdot 10^7$ wavelengths in size in just 1.4 hours by solving over two GPUs. This result

is a factor of 1.93 increase over the largest possible simulation on a single GPU without domain decomposition.

Our decomposition framework hinges on the ability to split the linear system as $A = L + V$. Instead of the traditional splitting, where V is a scattering potential that acts locally on each voxel, we introduced a V that includes the communication between subdomains and corrections for wraparound artefacts. As a result, the operator $(L + I)^{-1}$ in the MBS iteration can be evaluated locally on each subdomain using a fast convolution. Therefore, this operator, the most computationally intensive step of the iteration, can be evaluated in parallel on multiple GPUs.

Despite the significant overhead of our domain splitting method due to an increased number of iterations and communication and synchronisation overhead, the ability to split a simulation over multiple GPUs results in a significant speed-up. Already, with the current dual-GPU system, we were able to solve a problem of $315 \times 315 \times 315$ wavelengths $13.2\times$ faster than without domain decomposition since the non-decomposed problem is too large to fit on a single GPU. Moreover, as we demonstrated in Section 4.2.2, there is only a slight overhead associated with adding more subdomains along an axis after the first splitting. This favourable scaling paves the way for distributing simulations over more GPUs or compute nodes in a cluster.

In this work, we have already introduced strategies to reduce the overhead of the domain decomposition through truncating corrections to only a few points close to the edge of the subdomain and only activating certain subdomains in the iteration. We anticipate that further developments and optimisation of the code may help reduce the overhead of the lock-step execution.

Finally, due to the generality of our approach, we expect it to be readily extended to include Maxwell’s equations [15] and birefringent media [16]. Given the rapid developments of GPU hardware and compute clusters, we anticipate that optical simulations at a cubic-millimetre scale can soon be performed in a matter of minutes.

6. Code availability

The open-source Python implementation of our method is available on GitHub [39].

7. Acknowledgements

This work was supported by ERC proof of concept grant number 101069402. We thank Vassilis Sarantos, Evangelos Marakis, Michael Ktistakis, Ioannis Zaharakis, Vasilis Papadopoulos and Tom Vettenburg for motivating discussions.

References

- [1] J.-M. Jin, Theory and computation of electromagnetic fields, John Wiley & Sons, 2015.
- [2] G. Osnabrugge, S. Leedumrongwatthanakun, I. M. Vellekoop, A convergent Born series for solving the inhomogeneous Helmholtz equation in arbitrarily large media, *Journal of Computational Physics* 322 (2016) 113–124.
- [3] G. Osnabrugge, M. Benedictus, I. M. Vellekoop, Ultra-thin boundary layer for high-accuracy simulations of light propagation, *Optics Express* 29 (2) (2021) 1649–1658.
- [4] K. Yee, Numerical solution of initial boundary value problems involving Maxwell's equations in isotropic media, *IEEE Transactions on Antennas and Propagation* 14 (3) (1966) 302–307.
- [5] A. Taflov, S. C. Hagness, Computational electrodynamics: The Finite-Difference Time-Domain Method, Artech House, 1995.
- [6] A. F. Oskooi, D. Roundy, M. Ibanescu, P. Bermel, J. Joannopoulos, S. G. Johnson, MEEP: A flexible free-software package for electromagnetic simulations by the FDTD method, *Computer Physics Communications* 181 (3) (2010) 687–702.
- [7] M. Nabavi, M. K. Siddiqui, J. Dargahi, A new 9-point sixth-order accurate compact finite-difference method for the Helmholtz equation, *Journal of Sound and Vibration* 307 (3) (2007) 972–982.
- [8] Q. H. Liu, The PSTD algorithm: A time-domain method requiring only two cells per wavelength, *Microwave and Optical Technology Letters* 15 (3) (1997) 158–165.

- [9] B. Fornberg, The pseudospectral method; comparisons with finite differences for the elastic wave equation, *Geophysics* 52 (4) (1987) 483–501.
- [10] E. S. Wise, J. Jaros, B. T. Cox, B. E. Treeby, Pseudospectral Time-Domain (PSTD) methods for the wave equation: Realizing boundary conditions with discrete sine and cosine transforms, *Journal of Theoretical and Computational Acoustics* 29 (04) (2021) 2050021.
- [11] D. Y. Heh, E. L. Tan, Dispersion analysis of FDTD schemes for doubly lossy media, *Progress In Electromagnetics Research B* 7 (2009) 327–342.
- [12] F. Zheng, Z. Chen, Numerical dispersion analysis of the unconditionally stable 3-D ADI-FDTD method, *IEEE Transactions on Microwave Theory and Techniques* 49 (5) (2001) 1006–1009.
- [13] J.-M. Jin, Concluding remarks on computational electromagnetics, in: *Theory and Computation of Electromagnetic Fields*, John Wiley & Sons, Ltd, 2010, Ch. 12, pp. 533–558.
- [14] V. Dwarka, C. Vuik, Pollution and accuracy of solutions of the Helmholtz equation: A novel perspective from the eigenvalues, *Journal of Computational and Applied Mathematics* 395 (2021) 113549.
- [15] B. Krüger, T. Brenner, A. Kienle, Solution of the inhomogeneous Maxwell’s equations using a Born series, *Optics Express* 25 (21) (2017) 25165–25182.
- [16] T. Vettenburg, S. A. R. Horsley, J. Bertolotti, Calculating coherent light-wave propagation in large heterogeneous media, *Opt. Express* 27 (9) (2019) 11946–11967.
- [17] M. Lee, H. Hugonnet, Y. Park, Inverse problem solver for multiple light scattering using modified Born series, *Optica* 9 (2) (2022) 177–182.
- [18] A. Kaushik, P. K. Yalavarthy, R. K. Saha, Convergent Born series improves the accuracy of numerical solution of time-independent photoacoustic wave equation, *Journal of Modern Optics* 67 (9) (2020) 849–855.
- [19] X. Huang, M. Jakobsen, R.-S. Wu, On the applicability of a renormalized Born series for seismic wavefield modelling in strongly scattering media, *Journal of Geophysics and Engineering* 17 (2) (2019) 277–299.

- [20] C. M. Rappaport, B. J. McCartin, FDFD analysis of electromagnetic scattering in anisotropic media using unconstrained triangular meshes, *IEEE Transactions on Antennas and Propagation* 39 (3) (1991) 345–349.
- [21] M.-L. Lui, Z. Chen, A direct computation of propagation constant using compact 2-D full-wave eigen-based finite-difference frequency-domain technique, in: 1999 International Conference on Computational Electromagnetics and its Applications. Proceedings (ICCEA'99)(IEEE Cat. No. 99EX374), IEEE, 1999, pp. 78–81.
- [22] A. Bayliss, C. I. Goldstein, E. Turkel, The numerical solution of the Helmholtz equation for wave propagation problems in underwater acoustics, *Computers & Mathematics with Applications* 11 (7-8) (1985) 655–665.
- [23] L. L. Thompson, A review of finite-element methods for time-harmonic acoustics, *The Journal of the Acoustical Society of America* 119 (3) (2006) 1315–1330.
- [24] R.-E. Plessix, A Helmholtz iterative solver for 3D seismic-imaging problems, *Geophysics* 72 (5) (2007) SM185–SM194.
- [25] S. Wang, M. V. de Hoop, J. Xia, On 3D modeling of seismic wave propagation via a structured parallel multifrontal direct Helmholtz solver, *Geophysical Prospecting* 59 (Modelling Methods for Geophysical Imaging: Trends and Perspectives) (2011) 857–873.
- [26] L. Valantinas, T. Vettenburg, Scaling up wave calculations with a scattering network, *Intelligent Computing* 3 (2024) 0098.
- [27] B. Papp, G. Kristóf, C. Gromke, Application and assessment of a GPU-based LES method for predicting dynamic wind loads on buildings, *Journal of Wind Engineering and Industrial Aerodynamics* 217 (2021) 104739.
- [28] Z. Cooper-Baldock, B. V. Almirall, K. Inthavong, Speed, power and cost implications for GPU acceleration of computational fluid dynamics on HPC systems, arXiv preprint arXiv:2404.02482 (2024).

- [29] Z. Chen, X. Xiang, A source transfer domain decomposition method for Helmholtz equations in unbounded domain, *SIAM Journal on Numerical Analysis* 51 (4) (2013) 2331–2356.
- [30] C. C. Stolk, A rapidly converging domain decomposition method for the Helmholtz equation, *Journal of Computational Physics* 241 (2013) 240–252.
- [31] L. Zepeda-Núñez, L. Demanet, The method of polarized traces for the 2D Helmholtz equation, *Journal of Computational Physics* 308 (2016) 347–388.
- [32] C. C. Stolk, An improved sweeping domain decomposition preconditioner for the Helmholtz equation, *Advances in Computational Mathematics* 43 (2017) 45–76.
- [33] J.-D. Benamou, B. Després, A domain decomposition method for the Helmholtz equation and related optimal control problems, *Journal of Computational Physics* 136 (1) (1997) 68–82.
- [34] F. Collino, S. Ghanemi, P. Joly, Domain decomposition method for harmonic wave propagation: a general presentation, *Computer Methods in Applied Mechanics and Engineering* 184 (2) (2000) 171–211.
- [35] M. J. Gander, F. Magoules, F. Nataf, Optimized Schwarz methods without overlap for the Helmholtz equation, *SIAM Journal on Scientific Computing* 24 (1) (2002) 38–60.
- [36] A. Toselli, O. Widlund, *Domain decomposition methods-algorithms and theory*, Vol. 34, Springer Science & Business Media, 2004.
- [37] J.-P. Berenger, A perfectly matched layer for the absorption of electromagnetic waves, *Journal of Computational Physics* 114 (2) (1994) 185–200.
- [38] V. Dolean, P. Jolivet, F. Nataf, *An introduction to domain decomposition methods: algorithms, theory, and parallel implementation*, SIAM, 2015.
- [39] S. Mache, I. M. Vellekoop, Wavesim [software], https://github.com/IvoVellekoop/wavesim_py (2024).

- [40] T. Vettenburg, I. M. Vellekoop, A universal matrix-free split preconditioner for the fixed-point iterative solution of non-symmetric linear systems, arXiv preprint arXiv:2207.14222 (2023). [arXiv:2207.14222](https://arxiv.org/abs/2207.14222).
- [41] M. Van Rossum, T. Nieuwenhuizen, Multiple scattering of classical waves: Microscopy, mesoscopy, and diffusion, *Reviews of Modern Physics* 71 (1) (1999) 313 – 371.
- [42] D. M. Young, *Iterative solution of large linear systems*, Academic Press, New York, 1971.
- [43] A. A. Samarskij, E. S. Nikolaev, *Numerical methods for grid equations: volume II Iterative methods*, Birkhäuser, 1989.
- [44] B. Bialecki, Preconditioned Richardson and minimal residual iterative methods for piecewise Hermite bicubic orthogonal spline collocation equations, *SIAM Journal on Scientific Computing* 15 (3) (1994) 668–680.
- [45] R. E. Kleinman, G. F. Roach, P. M. van den Berg, Convergent Born series for large refractive indices, *J. Opt. Soc. Am. A* 7 (5) (1990) 890–897.
- [46] G. C. Sherman, Diffracted wave fields expressible by plane-wave expansions containing only homogeneous waves, *JOSA* 59 (6) (1969) 697–711.
- [47] K. E. Oughstun, The angular spectrum representation and the Sherman expansion of pulsed electromagnetic beam fields in dispersive, attenuative media, *Pure and Applied Optics: Journal of the European Optical Society Part A* 7 (5) (1998) 1059.
- [48] J. T. Gostick, Z. A. Khan, T. G. Tranter, M. D. Kok, M. Agnaou, M. Sadeghi, R. Jarvis, PoreSpy: A Python toolkit for quantitative analysis of porous media images, *Journal of Open Source Software* 4 (37) (2019) 1296.